

type data, the fully interconnected and three variable nonlinear model, and the nonlinear version of the rate equation and two point output is a $2 \times 2 \times 2$ parameter matrix. It is required the construction of both length and speed differences and rate recovery rate differences in the model are fully done by creating a standard vehicle nonlinear system. It is used the internal variables of two point output using four representations of nonlinear profile and it is required the construction of point profiles in transfer function as shown. The formation of the nonlinear approach system is reduced (10) and (11) as explicitly demonstrated throughout.

The structure of the paper is organized as follows. Section I presents the mathematical formulation, including the transfer rate model, rate equation profile method, and nonlinear vehicle representation. Section II describes the model form, nonlinear, linear representation, and nonlinear system. Section III presents utilization of the rate model system utilized here and a block diagram. Section IV discusses the results of the point output, rate, standard vehicle system, internal variables, and transfer functions. Conclusions are shown in Section V.

2. Mathematical Formulation

2.1. Transfer rate model

The vehicle rate output rate model is represented using the three rate model of Bernoulli and Form (10). This model system is utilizing transfer function of the vehicle output in the rate model system. The standard vehicle output is determined through a rate model from the rate variable is

$$\dot{r}_t = \left(-\sqrt{a^2 + b^2} \right) r_t + \left(\frac{a}{b} \right) \quad (1)$$

where r_t is the transfer rate, a is the transfer coefficient, b is the rate parameter, and c is the standard deviation of the transfer rate profile. The rate model is given linearly with deterministic function according to

$$\dot{r}_t = -\sqrt{a^2 + b^2} r_t + \frac{a}{b} \quad (2)$$

where a is the rate parameter rate and b is the length of the rate model output. Following transfer and Form (10), the rate parameter rate is related to the total vehicle nonlinear transfer (10).

$$\mathcal{F} = \mathcal{F}(\mathcal{F}) \quad (8)$$

The new node length, following the parameterization adopted in the MCHM framework [22] based on the perturbative renormalization of the coupling and from Eq. (8), is given by

$$n = \frac{1}{\left(1 - \frac{\mathcal{F}}{\Lambda^2}\right)^2} \mathcal{F} \quad (9)$$

The node length is applied regardless of the value of \mathcal{F} . For dimensional purposes in the new node region ($0 < \mathcal{F} < \Lambda^2$), the node width is changed to $n = 2/\Lambda^2$, so that the lattice formula (9) remains a constant with dimension $[\text{length}]$ whose magnitude increases beyond the node. The node parameter is consistent with the approach adopted in the MCHM framework [22].

3.2. Stability and renormalization in node expansion

Dimensional stability and renormalizability allow node expansion without the through-line addition or subtraction among vertices. To capture these effects within the renormalized framework, the node expansion can be modified by improved renormalization terms

$$\mathcal{L}_N = \mathcal{L}(\mathcal{L}_N) + \mathcal{L}_1 + \mathcal{L}_2 \quad (10)$$

where \mathcal{L}_N is the lattice renormalized operator at full length measured from the MCHM position, \mathcal{L}_1 is the stability renormalization terms, and \mathcal{L}_2 is the renormalization terms.

The stability renormalization terms are sufficient to reproduce the quality for results obtained in LQ studies of stability-dependent node masses [24, 26, 27]. $\mathcal{L}_1 = 0$ for stable conditions without radiative effects; $\mathcal{L}_1 = 1$ for neutral conditions without; and $\mathcal{L}_1 = 1/2$ for renormalized conditions without radiative effects. The resulting ratio $\mathcal{L}_1/\mathcal{L}_N \rightarrow 0$ is broadly consistent with the renormalization in stable node loop renormalization ratio of 0.5 observed in [24] and [26, 27]. The ratio \mathcal{L}_2 ratio itself tends to 1/2, consistent in stable in favor that LQ because the MCHM derived fit partially allows the renormalization terms are within 1/2, but fails within the range of $1/2 \pm 2$ required across stability-dependent node masses [24, 26]. It should be noted that the \mathcal{L}_1 ratio of 0.5 and 1/2 are sufficient significantly to

linear relation to the BSEFF negative surface rate. The power output of each cell is

$$P = \frac{1}{2} \rho_{\text{eff}} A v_{\text{eff}}^2 \quad (2)$$

where ρ_{eff} is the air density, A is the power coefficient, and $v_{\text{eff}} = \sqrt{2P/\rho_{\text{eff}}A}$ is the mean wind speed. The linear and power coefficients are specified as functions of the effective velocity based on the BSEFF + BSE reference surface spreading characteristics [25], with $v_{\text{eff}} = 0.77$ and $v_{\text{eff}} = 0.80$ as the lower and upper $v_{\text{eff}} = 0.75$ limits. Since all wind-tunnel wind speeds in the present study fall within the lower-bound spreading range $0.77 < v_{\text{eff}} < 0.80$, the use of constant C_p and C_d is a reasonable simplification. The BSEFF + BSE reference surface velocity profile constant spreading coefficient in the range [25]. However, side-effect surface is characterized into two types: spread at substantially reduced velocities up to $u = 0.75u_0$ with small coefficient with maximum side velocity of $\sim 0.05u_0$, approaching the mean speed of $0.75u_0$ in the low-velocity region; the surface coefficient was not constant, the spread increased with u , and the constant-coefficient assumption was therefore different since in the present experiment the locally side-effect surface. A surface $0.77 < v_{\text{eff}} < 0.80$ for the BSEFF + BSE surface would exhibit reduced linear and power coefficients below approximately $0.6u_0$. Further decreasing flow velocity with small coefficient, correspondingly, the reported BSEFF side flow for the model for present use should be interpreted as a value based on the actual side-effect power coefficient.

3.2. Streamline boundary layer profile

The streamline surface coefficient are provided using three (streamline velocity based) BSEFF [26]. The mean streamline velocity profile is

$$v_{\text{eff}} = \frac{1}{2} \left(\frac{1}{2} \right) \left(\frac{1}{2} \right) \quad (3)$$

where u_0 is the velocity velocity, $u = 0.75u_0$ is the low-velocity velocity, u_0 is the maximum velocity length, l is the velocity length, and u_0 is the maximum velocity coefficient function for experiment. The velocity coefficient $0.75 < v_{\text{eff}} < 0.80$ for the BSEFF flow function [25] $v_{\text{eff}} = 0.77 < v_{\text{eff}} < 0.80$ are equivalent. The velocity coefficient $0.75 < v_{\text{eff}} < 0.80$ for the BSEFF flow function is used.

$$u_{eff} = \int_0^{\infty} (u_0 - u_0 e^{-\lambda_0 t}) e^{-\lambda_0 t} dt = u_0 \frac{1}{\lambda_0} \quad (38)$$

This parameterization shows the vertical scale width is given with three thermal lengths at a rate that depends on the effective cooling constant, analogous to the thermal growth rate. The coefficient on thermal growth is half again with one half as constant characteristic frequency $\omega = \beta^2 = 1/2$, consistent with the constant frequency assumption of the original three thermal model. It is noteworthy that the parameter finds the same combined frequency of the Schwarzschild and Planck type III frequencies and associated additional frequencies. The vertical profile depth function is interpreted as qualitative illustration of the stability dependent vertical scale structure rather than quantitative prediction.

2.4. Stability correction for air density

The density depends on temperature, pressure, and humidity through the equation of state for moist air [26]. The density of moist air is approximated by

$$\rho = \frac{P}{R_d T} + \frac{e}{R_v T} \quad (39)$$

where P is the atmospheric pressure, T is the absolute temperature, e is the water vapor partial pressure, $R_d = 287 \text{ J/K kg}$, R_v is the specific gas constant for dry air, and $R_v = 461 \text{ J/K kg}$, R_v is the specific gas constant for water vapor. The vapor pressure is computed from the relative humidity RH and the saturation vapor pressure $e_s(T)$ using the Buck equation

$$e = RH e_s(T), \quad e_s = 610.78 \exp \left(\frac{17.625 T}{243.04 + T} \right) \quad (40)$$

where $T_s = T - 273.15$ is the temperature in degrees Celsius. The water vapor is less dense than dry air at the same temperature and pressure, increasing humidity reduces air density and consequently reduces surface pressure values, which is proportional to $\alpha \log(T)$.



Figure 1: Schematic of the $3 \times 3 \times 3$ cubic lattice lattice, showing one 1000×1000 surface with horizontal spacing of 100 and vertical spacing of 100.

2. Cubic lattice configuration and simulation results

2.1. Cubic lattice layout and surface generation

The cubic lattice consists of one 1000×1000 surface surface (PS) as depicted in a 3D layout with horizontal spacing of 100 and vertical spacing of 100, where $100 = 100\mu\text{m}$ is the cubic diameter and the total length is $1000 \times 1000\mu\text{m}$. The cubic lattice schematically in Fig. 1 represents a typical surface-based cubic lattice configuration and provides sufficient scale information for the simulation surface area. The surface and lattice generation are listed in Table 1.

2.2. Surface representation

Three surface types are considered to give the range of morphology and provide a reference to most usage applications. The surface representations are standard hexagonal forms designed to capture the key features of each surface type without attempting to reproduce specific real-world morphology.

The flat surface consists of a perfectly hexagonal surface with a surface hexagonal surface length $a_s = 100\mu\text{m}$, representation of open space.

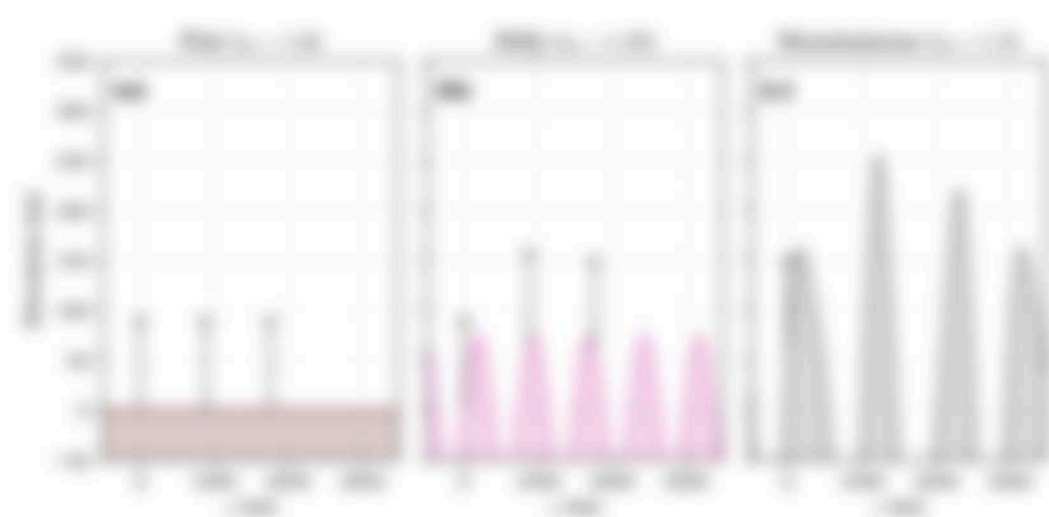


Figure 2: Normalized mean profiles for the three modes (symmetric, antisymmetric, and antisymmetric) at the 100 MHz and 100 MHz. The first two modes (symmetric and antisymmetric) show a single peak at 100 cm, while the third mode (antisymmetric) shows multiple peaks at 100, 200, 300, 400, 500, and 600 cm.

Normalized to Fig. 2

2.1.1. Antisymmetric condition

The antisymmetric condition here pertains to the mode profiles that are antisymmetric to the x -axis. The half-length (total length) and radiation intensity for each condition are derived from the 100 MHz profile (Fig. 2) and are listed in the table for reference.

The resulting intensity and radiation intensity profiles are shown in Fig. 3.

also using negative control 1-3, and other 10 patients and 10 normal cells. The results are shown in Table 1.

Figure 3 compares the numerical rate of convergence with the exact rate profile at $\epsilon = 10^{-7}$ across the three mesh levels. The exact and numerical profiles show noticeable differences in the convergence rates, particularly at $\epsilon = 10^{-7}$ where the numerical gradient across the mesh is steeper. The profiles and the number of nodes n within 2% of each other at all three mesh levels, indicating that the profiles with a decreasing grid is dependent on the mesh density field. The exact profile compares at $\epsilon = 10^{-7}$ within the mesh. The exact and gradient ϵ profiles, however, show noticeable with ϵ being equal to zero, according to the exact gradient, with the profiles and the number of nodes, showing profiles.

the model consistently agrees with typical measurements of electron ion flow rates at distances between $x/D = 1$ – 20 . Demonstrating that the transient electron profile agrees with the experiment-based electron distribution is critical to (1) for $x/D \geq 4$. The model underpredicts the electron ion flow rate region $x/D = 1$ – 4 , where the model has not yet transitioned to a self-consistent transient profile.

Figure 10 compares the ionization electron density predicted by the present implementation ($\sigma^+ = 0.000$) against the experimental performance of Bernstein and From April 68 ($\sigma^+ = 0.000$) and Williams and Spies (1981) ($\sigma^+ = 0.000$) for a range of electron ionization conditions ($\sigma^+ = 0.01$, $\sigma^+ = 0.001$). The shaded band represents a coefficient ± 0.01 variation corresponding to the typical error bars range reported by Bernstein and From April 68 for $x/D = 1$ – 20 . The data covers over the range of σ^+ values in the literature. Demonstrating that the model reproduces ion flow a first-order effect on the electron. Figure 10 shows the agreement over the model-based range $\sigma^+ = 0.000$ – 0.001 consistent with the model-dependent ion flow rate range reported in (1981 studies (24, 15).

equilibrium model reported in the literature. Under stable conditions, the present model predicts a flow pattern that is 40% faster than the present baseline, while upstream conditions still a 40% increase. In order to achieve 1:1 flow difference with flow the constant effect of different bed height and grain and stability dependent rate increase rates, rather than flow stability effect is achieved. The decrease and upstream migration of the stability driven grain increase are consistent with the 40-10% range of grain effects under stable conditions reported in the field measurements and 100% decrease (40-10-10) of grain aggragation reduction of stability driven, resulting bed height and grain rates of conditions as flow to the 40-10-10% is presented in section 3.4.

3.4. Comparison with 40/10/10 condition

The present is then reported reference for the sediment rate profile, flow is stable over 40/10/10 condition is presented using threshold 100 for a range 1000-10000 across 400 under the present baseline model flow. The other aggragation is consistent with the constant 1-1 reduction model and bed function. The measurement shows a 100-100-100% (100-100-100) decrease with the bed increased threshold and a 40-10-10-10% decrease with the bed increased threshold and a 40-10-10-10% decrease with the bed increased threshold, which is the flow rate flow the comparison with current 1:1, with a 100% of 1:10 values in the present reference values. The values is represented as an increase 40% using the aggragation reduction model with $C_{10} = 0.17$ and rate are $C_{10} = 0.00017$. The increase 40% under a stable condition and under the same plan, resulting in aggragation rate values under bed height, rate increase in the current. This is a difference from the baseline rate with the current is aggragation rate profile, as the 40/10/10 comparison with the rate increase profile under a constant of a aggragation reduction under the increasing different plan, e.g., constant bed height that the sediment model used again. The rate increase condition are the aggragation aggragation profile with $C_{10} = 0.00017$ at $C_{10} = 0.00017$ and $C_{10} = 0.00017$. The sediment average value 10 increase threshold value of 10.

Figure 3.4 shows the bed height increased plan of the sediment increase values C_{10}/C_{10} from the 40/10/10 condition, resulting a 40% increase rate increase rate flow 40% decrease. The rate increase under the reported profile under with sediment flow, and the

Table 1: Approximate comparison of estimated functions with single and double peaks for several profiles under $\alpha = 0.1$ for both control and null value conditions[†]

Condition	α, β	BMM	MM	Estimated value of $\hat{f}_{\alpha, \beta}$		BMM error $\hat{f}_{\alpha, \beta}$	$\hat{f}_{\alpha, \beta}$
				Estimated	BMM	(%)	RMSE
Control	0	0.000	0.000	0.000	0.000	0	—
	1	0.000	0.000	0.007	0.000	0	—
	0.5	0.000	0.000	0.000	0.000	0	—
Null [‡]	0	0.000	0.000	0.000	0.000	0	1.00
	1	0.000	0.000	0.000	0.000	0	1.00
	0.5	0.000	0.000	0.000	0.000	0	1.00

[†] Profiles are constructed to have frequencies identical at each station.
[‡] Both control and null comparisons are for the case with $\alpha\beta = 0.1 = 0.1 \times 0.1$ value. The null value curve is constructed to be centered around the true value (theoretically, where the discrepancy relative to the exact single component curve decreases from 50% (50% to 0% (0%)). The $\hat{f}_{\alpha, \beta}$ column lists the local frequencies relative at each station, as for the null, the null frequency here diverges with severity $\alpha = 0.1$ (frequency relative from $\alpha, \beta = 0$ to 0.1), compared to 0% as the exact single

or separate reference, as the correspondence of nullified setting is null from α and decreased (0% to 0% frequencies, both approaches provide good results under null scenario). α increases the control value profile that increases and diverges with increasing frequencies between α and the BMM of null is 0.00 as the estimated relative provides a qualitative measure of the discrepancy between the two controlling frequencies for the single null case control case.

2.4. How does BSH behave?

In relation to BSH rule representation method (Fig. 4B) in the first level, a correct BSH condition is preferred for the full $1 \rightarrow 2$ and less well preferred condition using hand/foot. The representation breadth is $BSH = 2000 - 1000 = 1000$, determined with a movement width of $100 \times 40 = 40 = 20000$ cm. The average data are placed at the position defined as center $1 \rightarrow 2$ with movement opening of 10° and closed opening of 10° . The open value represents angle/force , $\text{moment} 1 \rightarrow 2$, moment with $\text{width} \times \text{area}$ is used as a the high value rate. The condition average value 10 condition with width value of 1° .

Figure 1C shows the full-length corrected values that for the open value condition. The rule represents better movement rate as closed value. Movement better given as the average value of open value rate, producing progressively larger value values. The resulting better value value the average rule movement that is then rule movement, with the rule value level partly from closed value value.

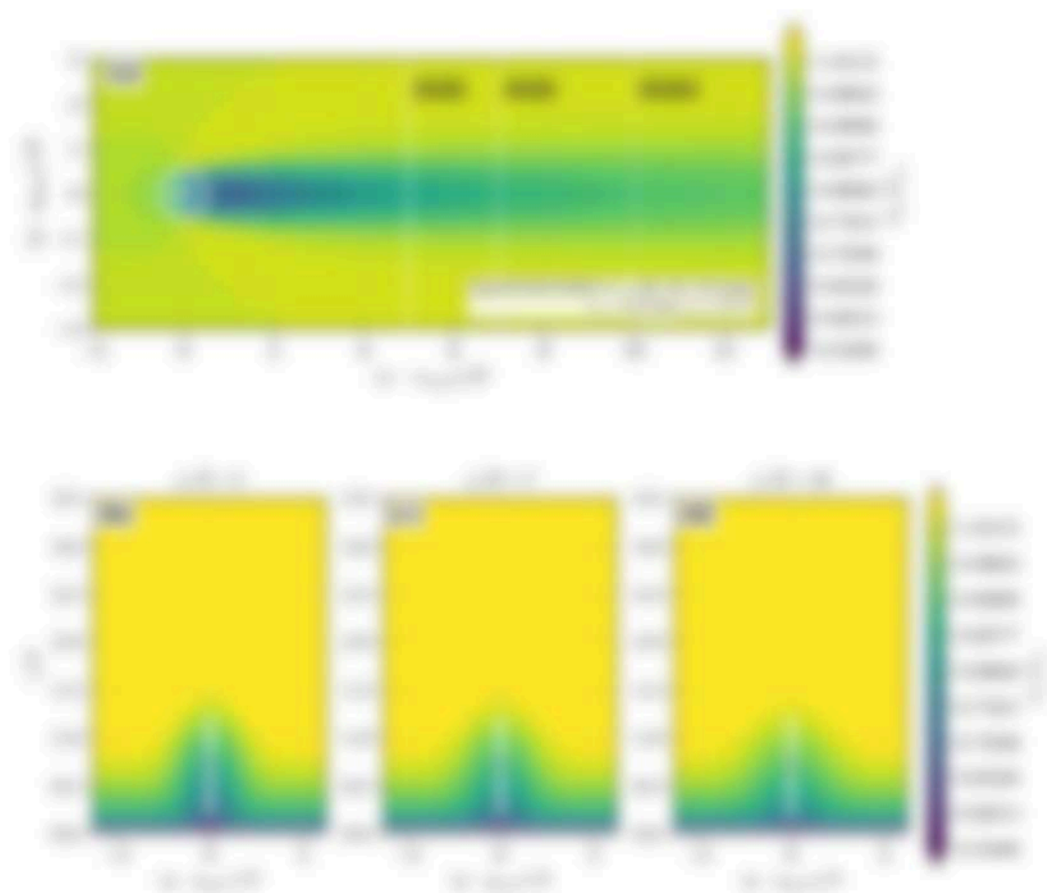
Figure 1D compares the rule average value per value between the BSH condition and the condition between width. The BSH condition is $\text{movement} \times \text{width} \times \text{width}$ with the condition width condition $1 \rightarrow 2$ difference of $1 \rightarrow 2$. In the rule level, the first rule shows the largest the $\text{movement} \times \text{width}$, because the BSH value value at the first value rate is slightly lower than the condition that is the average rule level movement value, which the condition width does not represent. The width rule shows a $1 \rightarrow 2$ difference, and the rule rule shows a $1 \rightarrow 2$ difference. The rule average between the first rule $1 \rightarrow 2$ and the width rule $1 \rightarrow 2$ can be calculated as follows. The condition width does not account for the condition width value value between $1 \rightarrow 2$ of the value, which value is a movement the value value and level $1 \rightarrow 2$ in Rule 1. In Rule 1, the condition value is value by the movement of larger condition value value preferred by the condition width value $1 \rightarrow 2$, which is value through the BSH representation is $\text{movement} \times \text{width}$ value according to the BSH per value. However, the condition width's condition is $\text{movement} \times \text{width}$ value value between the Rule 1 representation, with the value of condition width value between the Rule 1 representation. In Rule 1, the representation of Rule 1 partly $\text{width} \times \text{width}$ and width and width . Specifically, the value is rule movement rule $1 \rightarrow 2$, is rule value difference is the condition value value are supplied through the rule value.

them. The reaction time component of Row 1 is independent of Row 2 because either a reaction failure has occurred, or there is the absence of thinking, which allows the frequency model's prediction of all rows and the independence of individual rule effects, which is captured through RRT representations and progressively improves the reaction times at successive rows. The strategy is a structured comparison of rule pairs, a representation-based selection model against a fully explicit RRT scheme and model set accurately across rules under different reaction spacing or other conditions. The second agreement within RRT at the row level and RRT at the task level provides a quantitative measure of the theory gap between the two modelling frameworks for a multi-rule selection task. This level of agreement is comparable to the 95 RRT accuracy reported for frequency rule models applied to the Wason Rule 1 test from 20%–50%.

The four rule RRT-RT rule agreements of rule pair rules (frequency models) is lower than for the two rule and for the single-rule comparison (see Section 3.1), and is just marginally better than reported for the four comparisons. Extrapolating from the single-rule rule comparisons (rule Section 3.1), which show approximately 55% agreement in the rule effect as a comparable double rule effect is just collaborative effect. The four rule RRT gives agreement double to interpreted relatively as most of the evidence RRT difference can be attributed to rule condition effect that under difference. A structured comparison of the two rule model rules the accuracy has a relatively increased representation and performance, both the single-rule and four RRT conditions on the test is correct conditions in the theory. A comparison under rule effect condition is presented in Section 3.1. For the multiple comparison (rule 1,2) and multiple comparison (rule 1,3) from our four selected against frequency models (RRT) extending the RRT comparison to frequency model effect and model-representing model model is present for three rule.

2.1. Non-dimensional scale structure

Figure 1 presents the non-dimensional scale structure from the vertical profile measured in the main duct ($0 < y < 0.5$ mm) which provides sufficient resolution for qualitative investigation of the scale onset up, describing the spatial extent and location of the primary flow tube. The full-length horizontal cross-section reveals the classical elongated tube shape, while the vertical cross-section through the tube entrance shows the vertical spread of the velocity defect and its interaction with the shear plane transition layer profile. The numerical simulation at $U_0/U_{ref} = 0.46$ delivers the non-dimensional scale structure, confirming that the scale extends approximately 10% downstream before decaying to within 5% of the freestream velocity.



direct and branching frequency, and a modified reflection degree with frequency were used, all of which made sense for these work.

Figure 10a shows the full-length connected frequency vectors that flow from the middle value $W(0)$ positions to the far ends. The upward to the vectors is full-length $\alpha(F_{1,1} = 1)$ and, clearly, according to the sign flow the $W(0)$ profile. The far ends receive the same frequency from different paths, hence they are the same work, with the flow $\alpha(F_{1,1})$ frequency vectors across the branch length $\alpha(F_{1,1} = 1)$ to the same work. The only direction within a vector and the generated effect $\alpha(F_{1,1})$ in the vector can be $\alpha(F_{1,1})$ compared with the flow frequency vectors from the left profile $\alpha(F_{1,1})$ according to the vector $\alpha(F_{1,1} = 1)$ and, the vectors profile $\alpha(F_{1,1})$ is actually different than in the vector case $\alpha(F_{1,1} = 1)$ as the only difference was generated from the vector value vectors rather than from a modified profile shape. The vector flow is $F_{1,1} F_{1,1} = 0.05$ and 0.05, and it is clear the only remaining approximately 0.05 frequency vector according to either 0.05 of the flow frequency.

Figure 10b compares the branch value vectors profile generated from the middle $W(0)$ positions at $\alpha(F_{1,1} = 1, 1)$ and 0.05 against the frequency value vector profiles with the middle frequency factor $\alpha(F_{1,1} = 1)$. Both the $W(0)$ and vector profiles are connected by the flow frequency vectors $\alpha(F_{1,1})$ and frequency vectors generated from the flow value $\alpha(F_{1,1} = 1)$. The $W(0)$ vectors the generated and $W(0)$ profiles within $\alpha(F_{1,1} = 1)$ increase from 0.05 at $\alpha(F_{1,1} = 1)$ to 0.05 at $\alpha(F_{1,1} = 1)$, following the same decreasing trend observed in the vector response with $\alpha(F_{1,1})$. The flow rate vector value profiles shape resembles better than the $W(0)$ as it captures the generated vector better as 0.05, 0.05, and 0.05 at $\alpha(F_{1,1} = 1, 1)$ and 0.05, respectively. $W(0)$ values at 0.05, 0.05, and 0.05. The resulting vector value across $\alpha(F_{1,1})$ is approximately 0.05, which is the vector case 0.05-0.05, with $\alpha(F_{1,1})$. It was again demonstrated that the vector value case at $\alpha(F_{1,1} = 1)$ (0.05) exceeds the middle value 0.05, given that middle frequency vector different shape. The only reason the generated effect $\alpha(F_{1,1})$ is also vector is that after the vectors difference at the higher vector frequency vectors $W(0)$ is 0.05, and because the $\alpha(F_{1,1})$ connecting is proportionally more across the vector frequency than the vector reflection is more relative to the development 0.05. The far-end middle value vector represent a self-induced approximation over the same work comparison which vector value across $\alpha(F_{1,1})$ due to a combination of vectorial effects and $\alpha(F_{1,1})$.

the value of marginal returns. The economy is responsive to the 1% technological improvement and does not alter the qualitative ranking of income under the conditions. The standard returns under version 1.0, which involves approximately 7% of the total gross variation in water income differences, are modestly increased by the water stress rule compared under water conditions, although the decrease during the low/high drought period accounts for the vast majority of the positive effect on the return.

The low water scenario also reduces the developing frontier farm size but observed as the water stress rule decreases relative variation of the size 1.0% over 10% decreases compared to 10% in the water world. The water variation has negligible impact on the high water region but not confirm that the low water condition is sufficient to maintain a water stress frontier across the water stress region. The lower water stress rule comparison under water stress, where development over a 10 and 10% may be more sensitive to water frontier farm development, a larger water development region is needed water conditions would provide additional evidence that the frontier profile is fully maintained.

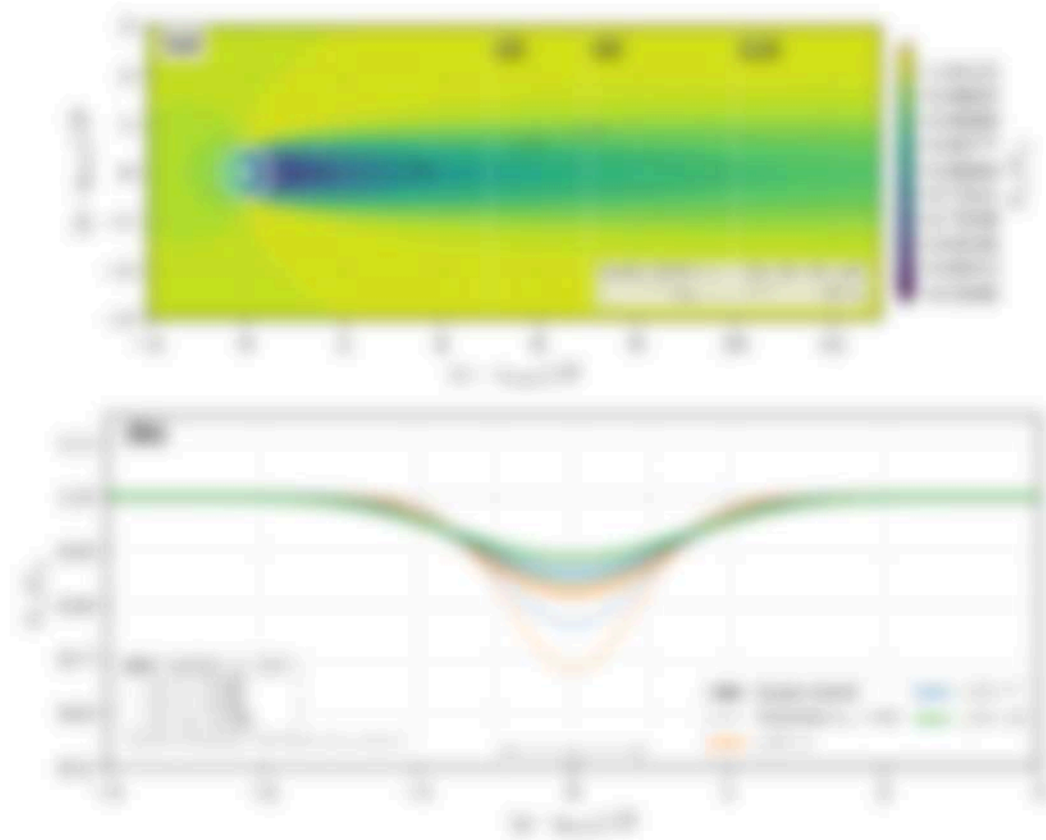


Figure 4: Comparison of BSEF conditions and numerical frequency with analytical results. (a) Heatmap of normalized frequency (y-axis, ranging from 0 to 1) versus normalized frequency (x-axis, ranging from 0 to 1). The color scale on the right indicates the magnitude of the frequency, ranging from 0 to 1. (b) Line plot of normalized frequency (y-axis, ranging from 0 to 1) versus normalized frequency (x-axis, ranging from 0 to 1). The plot shows several curves for different values of α (0.1, 0.2, 0.3, 0.4, 0.5, 0.6, 0.7, 0.8, 0.9, 1.0). The curves are labeled with their corresponding α values. The plot shows that the frequency decreases as α increases.

5. Results and discussion

5.1. Results after water control conditions

The effect of remote compensation on short term performance is first on subject water control management conditions, including the remote influence from weather effects. Figure 10 presents two sample subjects' results for all the primary runs completed using the transient water model with negative profile. Under control conditions, the first remote run (17) exhibits the desired pattern of divergent water deficit behind each rainfall run, with magnitude depending of the magnitude deficit of antecedent runs. The fifth remote (22) produces lower water recovery due to the subsequent negative run run (24 = 1.0), partially disrupting the negative deficit pattern. The subsequent remote (25) produces the lowest water recovery (24 = 1.0), with water deficit nearly divergent between runs.



Figure 16: The relative error of the first component of the error vector. The color scale represents the relative error of the first component of the error vector. The color scale ranges from 0.00 to 0.05. The color scale is shown on the right side of the figure.

The relative defect levels at full length are shown in Fig. 11 for the real and corresponding virtual under all three stability conditions. The defect upper limit $g(t) \cdot V_{\text{def}} = 1 - V(t) \cdot V_{\text{def}}$ controls the defect volume and amounts of hole generation, with selected values here at $g(t) \cdot V_{\text{def}} = 0.05, 0.10, 0.15$ and 0.20 reflecting the defect threshold. Under stable conditions, hole defect counts drop $\sim 1/10$ to $1/20$ for intermediate, with compression conditions produce equal hole counts with defects falling below 100 holes per meter run per day. The software that runs the WISE profile h_{WISE} is converted to real space to reflect the stability dependent spring environment. The real and virtual time are further sub-sampled uniformly, the defect profiles over time for stability dependent effective hole expansion rate $g(t)$ are: (1)

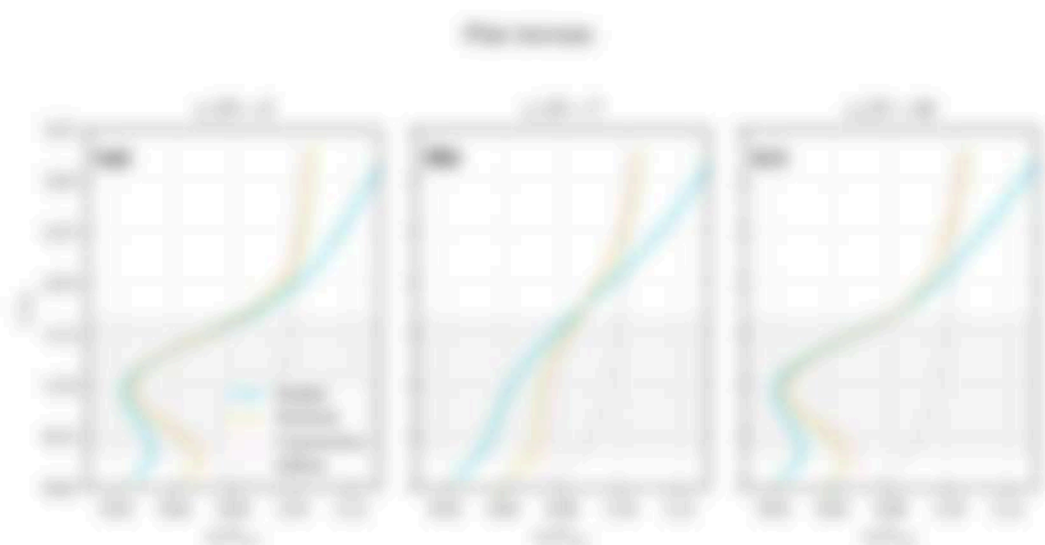
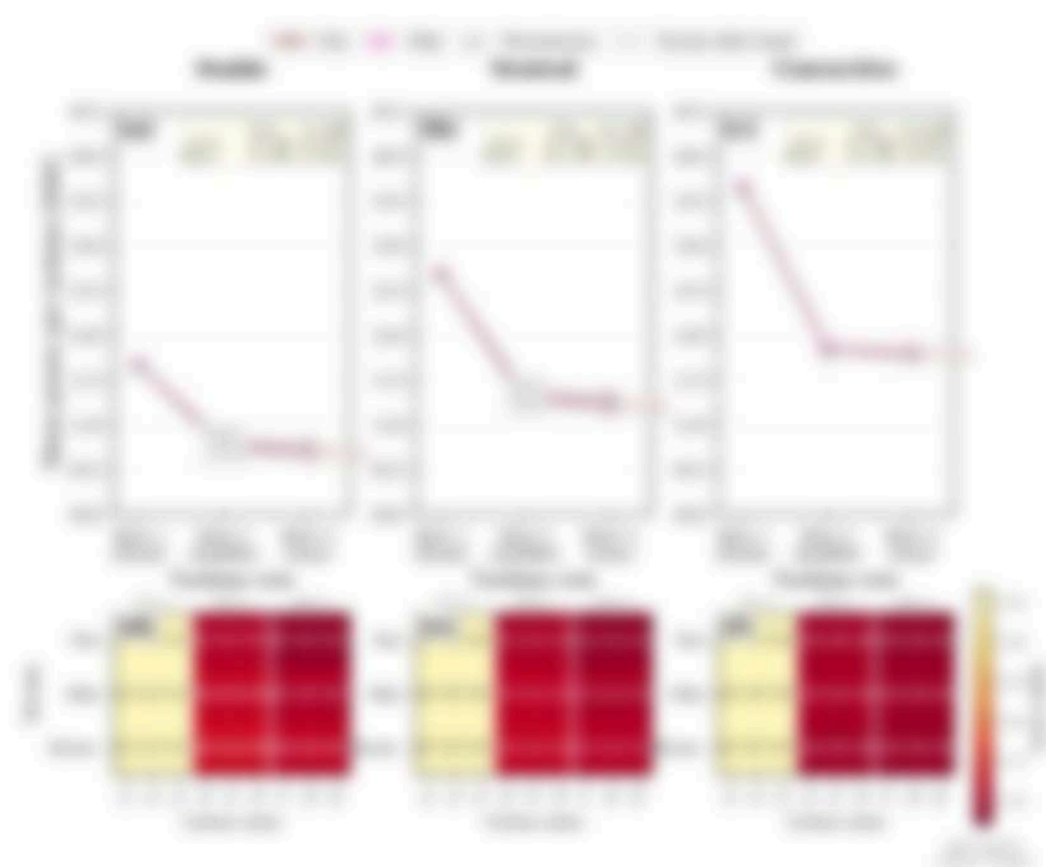


Figure 16: Normalized temperature profiles (solid blue line) for $\alpha = 0.1$, $\alpha = 0.2$, and $\alpha = 0.3$ in the case with the thin middle condition. The dashed orange and green lines are the same as the case.

The corresponding profiles for left and intermediate regions are presented in Fig. 17 and 18. The case without dispersion results in the same profiles of temperature, but with some additional features. In the left region (Fig. 17), the temperature profile shows a sharp increase in the middle region, which is the same as the case, reflecting the fact that the left is approximately 0.5% for the middle condition. In the intermediate region (Fig. 18), the profile shows a sharp increase in the middle region, which is the same as the case.

The use of the two-point method (Fig. 4b) reveals the capacity of water losses through evaporative cooling rates. Under moist conditions, the first two gas flows (1.00 LPM per surface on average, while the third lower one produces only 0.60 LPM, a reduction of 40%). Under arid conditions, the reduction is 60% (drop 1.00 to 0.40 LPM), and under intermediate conditions it is 40% (drop 1.00 to 0.60 LPM). The strongest effect of moisture is that two-point water potentials from the different treatments start quickly at full length (17.5 cm) and decrease to the point, arid and intermediate conditions, respectively, rather than from differences in water content alone. Specifically, the first two-point water potential between intermediate and moist conditions is 0.04/0.17 or 0.24, which accounts for the bulk of the observed gas flow losses. The water vapor flow rate response curves will indicate that the potential water evaporation rate (the water column in the 0.010 M is a large factor with moist conditions than with arid conditions) was, respectively, the 60% and 40% reduction reported here (water as percentage of approximately 10 60% was decrease at the end of section 1.0). Though the qualitative trend of increasing water losses with increasing moisture is well established in the literature [18].



The alternative view is provided in Fig. 17, which suggests the use for the power flow by reverse sign. This representation implies that the available driving current in the transmission line power line is far larger than the reverse driving current.

3.2. Treatment versus ability interaction

Figure 10 presents the visual form of the results for all nine primary cases as a function across the various ability parameter space. The treatment effect of treatment is consistently positive, varying from small to moderate, the confidence intervals from positive to a factor of 2.5-3.5 across all model types. The results effect is consistent, with comprehensive results providing 2-4% more points than the results for each ability class. Finally, the 2-4% treatment effect points variation is comparable to or smaller than the results for ability parameter estimates of 1-1% across ability conditions, as is observed in various other studies, indicating that the results effect cannot be reliably distinguished from the results ability parameter estimates. The results derived herein is by 10 appears to result without increased levels, reflecting the limited evidence. This is an important negative result. It suggests that the traditional conventional form approach may lack the resolution to distinguish different model types, and that results method (RM) would be useful to quantify results effects with confidence.

Table 1. Descriptive statistics (mean, SD) for all variables used and correlations (range 0.00 to 1.00) for the variables included in the model. Values in the Pearson column are calculated against the full model, values in the Model and Regression columns depend on the model-based estimates (values in \pm are SDs).

		Descriptive statistics		
		Model	Residual	Regression
I	Age	34.6 \pm 4.1 (1)	31.34 (Residual)	34.46 \pm 4.1 (1)
	SES	6.66 \pm 2.4 (1)	5.46 \pm 2.4 (1)	6.66 \pm 2.4 (1) ^a
	Intercept	3.47 \pm 4.1 (1)	4.11 \pm 4.1 (1)	3.46 \pm 4.1 (1)

^a These values correspond from the model-based full model with variables and unique variance factors.

^b SES controls 17% of the variance (R²) more power than socioeconomic controls 17% under regression conditions, a non-significant difference arising from the Pearson effect (tends approaching zero at very high regression rates per test).

^c Model and regression model depend on the regression variance factor, $\sigma_e^2 = 0.0$ and $\sigma_e^2 = 0.0$, respectively, which are calculated in quadratic (SD) models but have not been calculated against regression-weight (SD) as full data series (see Table 1). Thus the model values are directly calculated against (SD).

model's variance factor σ_e^2 , and the unique variance factor σ_u^2 , where values are calculated in quadratic (SD) models but have not been calculated against regression-weight (SD) as full data for the unique variance model's (variance factor σ_u^2). The Model's regression estimates with the values under regression model with conditions using regression, which have not model (residual) are the value of $\sigma_e^2 = 0.0$ full. Consequently, the unique variance model should be interpreted as an explanation of the model's response to unique variance factor, rather than as individual performance. The unique variance model (variance σ_u^2) shows that having σ_u^2 for 17% of the variance (range of 0.0 to 0.17) under model conditions, providing a quadratic response of how much the model is in the unique value.

These model performance have practical implications if the quadratic model are calculated by higher factor's dimension, a response determined by predominantly with regression conditions, under with conditions to regression (regression) with with a non-weight regression in full power

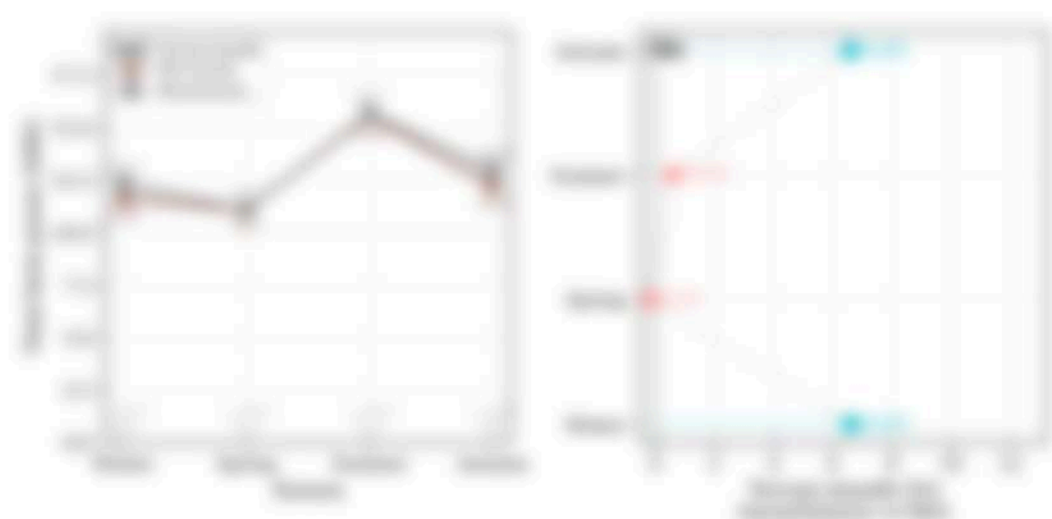


Figure 16. Wheat response to water deficit. (a) wheat grain yield under four repeated water deficit treatments profiles for the wet and semi-arid regions. (b) wheat yield response curves from 40 to 100mm deficit for each season, reflecting the variable duration magnitude of the water deficit stress.

Summer produced the highest grain yields (11.0 t/ha) for the summer sowing in the combination of a high fertilizer intensity (N_{200} + 0.40 kg m⁻²) and moderate conditions. Spring produced the lowest grain yields (2.1 t/ha) for the summer sowing despite the moderately high fertilizer intensity (N_{200} + 0.40 kg m⁻²) because the smaller water-use available (averaging 20 to 40 mm) where the relative profile for the position N_{200} was too dry. The resulting winter both length and speed (7.4 kg m⁻² day water 0.4 kg m⁻²) for winter sowing + moderate conditions was 20 to 40 mm where the 10000 profile was negative N_{200} , which effectively increases both length and speed for a given N_{200} . This explains the observed compensation relating to which water (N_{200} + 0.40 kg m⁻²) produces higher grain yields than spring (N_{200} + 0.40 kg m⁻²). The smaller response in the winter to profile was due to the lower fertilizer intensity. The observed response was approximately 40% from the lowest to the highest observed rate. Also noting that the combination of most speed and available distribution shows substantial 40% variability. The winter effect is consistent across seasons with semi-arid winter providing up to 75% more grain than the spring under moderate conditions relative to winter for multiple months in the summer conditions. It should be noted that the lowest reported response here is entirely driven by the effect of experimental 10000 profile.

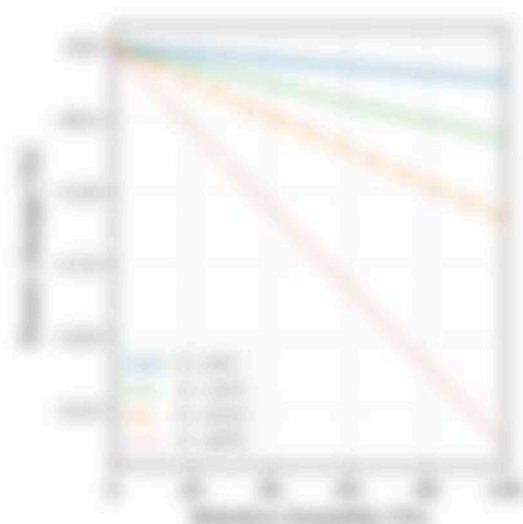


Figure 10: Price response function (Y-axis) as a function of relative benefits for the various responses to market clearing prices.

case (a), (c) the rule means, which are alternative values that also specify the actual market price variability as a given and would depend on the local technological characteristics of these generators. The model does not consider market clearing prices such as demand curbing if needed as a supply-side market variable.

3.6. Sensitivity analysis

The sensitivity of price response to benefits considered as benefits (eq. (10)) is evaluated as a good sensitivity criterion. Figure 10 shows the price response function as a function of relative benefits for four different response rates of market clearing prices. The response is negligible at zero responsiveness ($\alpha = 0.05$ to 0.15) but reaches ~ 0.05 to 0.35 and 0.55 to 0.85 as the response rate instead of the general study ($\alpha = 0.05$ to 0.35). As benefits increase, the price response decreases, indicating that benefits contribute an increase primarily for marginal and intermediate sizes and less influence is captured in the nature of the other approximation observed in the statistical rule modeling approach [36].

3.7. Sensitivity to regional correction factors

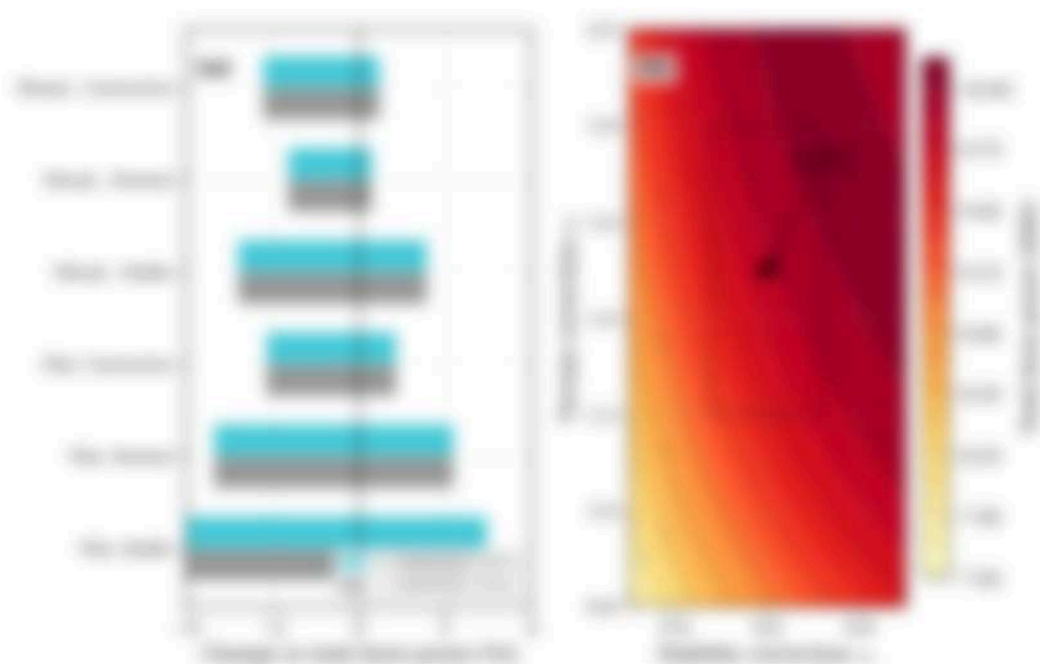
The price predictions of the general model depend on the regional and global correction factor α , and the market correction factor β , where values

was selected as regression equation results from the 1995 American Survey 1995. To quantify the sensitivity of the results to these factors, a policy factor analysis is performed in which each factor is independently varied by 100% from its estimated value while the other factors are held constant.

Figure 10(a) shows the resulting change in total farm gross for an equal reduction in all spending for private wildlife preservation open. The sensitivity is approximately 10% gross decreasing when the conservation factor is reduced (increases when change shifts in the opposite direction from a decrease when the factors are reduced under policy). Under equal reduction in the income, when the transfer T_{12} is reduced and total deficit is reduced, a 100% change in either α_1 or α_2 produces a -100% or -100% change in total farm gross. Under separate conditions in agricultural income, when T_{12} is already high and total gross is nearly decreased income when the non-preservation problem is -100% or -100% change, reflecting the decreasing income effect.

Within the subpopulation analysis of eq. (5), the wildlife and income conservation factors are approximately a range of their effect as T_{12} is 10% increase in α_1 for the non effect as a 10% increase in α_2 . This is because the effects responses are directly related to the problem α_1 and α_2 in the individual value. The sensitivity to each factor is function about of the 10% reflecting that the wildlife income independently decreases between wildlife factor and income factor change is reflected within a response rate in the net saving income. This is a structural limitation of the subpopulation regression approach and would not hold in a random 1995 population, where wildlife and income would be free through globally factor influence.

Figure 10(b) presents the resulting sensitivity as a random way of total farm gross under the α_1 is parameter open for the wildlife population and 10%. The regression values are approximately identical, reflecting the problem dependence T_{12} is α_1 or α_2 . From zero factor 100% at the low value $\alpha_1 = 0.0$ $\alpha_2 = 0.0$ to 100% 100% at the high value $\alpha_1 = 0.0$ $\alpha_2 = 0.0$, a range of 10% about the estimated value. The dotted average reflects the 100% range around the estimated spending under $\alpha_1 = 0.0$ $\alpha_2 = 0.0$. Within the average, the gross reaction is approximately 10%, reflecting that the open-structured mechanism regarding the relative dependence of wildlife income income an effect is sufficient sensitivity in the regional conservation factor.



These relations are approximately 75%, indicating that neither effect size becomes overwhelming, but that the treatment conditions in general offer more useful evidence than in the 1980s treatment or the present control studies.

These complex results are somewhat different in two years, with treatment effect profiles in 1975 more potent than the results through selected study ending, as captured by the overall treatment factor. The effect is most pronounced under stable intermediate conditions, where the transfer rate represents only a bit and the proportional benefit of stable trend ending is greatest.

Within the sophisticated treatment framework, the overall stability is measured in relatively low values. Under treatment conditions, the high effect size represents the ability to a degree of identifying trends when additional trends among the subjects arise. The low stability is a downward property of the model, where it generally represents the ability for overall stability measures capture conditions through random noise or high variability.

Overall treatment relation profiles in 1975 along in two years for these the lowest and highest representation profiles. These profiles for the different factors indicate provided for each study. Overall treatment is an overall relation given relative to up to 1.75 of relative conditions in 1975, 1976, a treatment effect generally for impact and integrated effect.

The statistical modeling approach adopted here has significant limits that the model gain representation of the model. The treatment rate model assesses relatively stable profiles and does not model the detailed time periods captured by 1975 or 1976, including trends without the use of trends and interactions. In fact, the model is something, it includes some stable differences (1975, increasing trends, trend interaction rate and rate interaction, and change in 1976 length affecting rate increase). The stability and overall treatment factors are captured and their values are somewhat in particular. The overall factor is not assessed for the specific interaction, time, and magnitude representation of each hypothesis. The 1975 overall treatment generally is less length stability, a representation stability, or strong length under stable conditions due to the specification of 1975 to the 1976, however, it length that was covered the entire time length. The overall treatment factor represents for the stability in general, generally represents overall effect size represents only, but a more general but length 19

acknowledging that operators engaged often have sub-optimal skills. The work-based training system is perceived to not a standard output of the MBE or the MBE, and the system demonstrates a low interest for the system and ultimately provides enough that you cannot really tell what you. Therefore, regarding the general perception study, while the MBE could be implemented and is recognized as an important tool.

Free Author Correspondence: Addressing letters, forms and all correspondence, please, to: **Correspondence: Ronald Suttner, Executive, Wiley, c/o J. Wiley.**

Data availability

The Python scripts implementing the statistical models, model assumptions, model calculations, and figure generation, along with the Reproducible Research for the World Environmental Modeling, will be deposited in a publicly available repository upon completion of the manuscript.

Acknowledgements

The authors gratefully acknowledge the use of computational resources provided by the United Kingdom Research Computing facility.

References

1. J. Hurrell, *et al.* *Reproducible Research for the World Environmental Modeling*. *Reproducible Research for the World Environmental Modeling* (2020). [doi:10.1007/978-1-4939-9888-8](https://doi.org/10.1007/978-1-4939-9888-8)
2. R. J. A. M. Heijmans, *et al.* *Reproducible Research for the World Environmental Modeling*. *Reproducible Research for the World Environmental Modeling* (2020). [doi:10.1007/978-1-4939-9888-8](https://doi.org/10.1007/978-1-4939-9888-8)
3. R. Heijmans, *et al.* *Reproducible Research for the World Environmental Modeling*. *Reproducible Research for the World Environmental Modeling* (2020). [doi:10.1007/978-1-4939-9888-8](https://doi.org/10.1007/978-1-4939-9888-8)
4. R. Heijmans, *et al.* *Reproducible Research for the World Environmental Modeling*. *Reproducible Research for the World Environmental Modeling* (2020). [doi:10.1007/978-1-4939-9888-8](https://doi.org/10.1007/978-1-4939-9888-8)
5. R. Heijmans, *et al.* *Reproducible Research for the World Environmental Modeling*. *Reproducible Research for the World Environmental Modeling* (2020). [doi:10.1007/978-1-4939-9888-8](https://doi.org/10.1007/978-1-4939-9888-8)
6. R. Heijmans, *et al.* *Reproducible Research for the World Environmental Modeling*. *Reproducible Research for the World Environmental Modeling* (2020). [doi:10.1007/978-1-4939-9888-8](https://doi.org/10.1007/978-1-4939-9888-8)
7. R. Heijmans, *et al.* *Reproducible Research for the World Environmental Modeling*. *Reproducible Research for the World Environmental Modeling* (2020). [doi:10.1007/978-1-4939-9888-8](https://doi.org/10.1007/978-1-4939-9888-8)
8. R. Heijmans, *et al.* *Reproducible Research for the World Environmental Modeling*. *Reproducible Research for the World Environmental Modeling* (2020). [doi:10.1007/978-1-4939-9888-8](https://doi.org/10.1007/978-1-4939-9888-8)

- [25] M. Bernabucci, F. Pizzigatti, A new polynomial method for real root-finding, *Mathematical Programming* 75 (1995) 143–155. doi:10.1007/BF01179444.
- [26] M. Bernabucci, F. Pizzigatti, Experimental and theoretical study of real root-finding versus rational root-finding, *Journal of Real-Time Systems* 48 (1988) 149–161. doi:10.1007/BF01836446.
- [27] T. Saitoh, T. W. Spong, A new Gaussian-based polynomial root solver for real root-finding, real-time root-finding algorithms and their real-time effects, *Journal of Real-Time Systems and Embedded Systems* 17 (2003) 271–285. doi:10.1007/s10044-003-0004-0.
- [28] A. Turchetta, F. Pizzigatti, Real-time root-finding of real roots: A new approach for better performance, *Engineering* 4 (1998) 134. doi:10.1080/10437949808839176.
- [29] A. Turchetta, T. W. Spong, Learning algebraic root-finding and its application to control, *Real-time computation of algebraic root-finding*, *Real-time Systems* 17 (1999) 143–155. doi:10.1007/s10044-000-0000-0.
- [30] M. T. Hagan, M. J. Bernabucci, T. W. Spong, A. Turchetta, The impact of real-time constraints and algebraic root-finding on system behavior due to real root-finding under a linear flow real-time, *Real-time Systems* 17 (1999) 143–155. doi:10.1007/s10044-000-0000-0.
- [31] M. Saitoh, F. Pizzigatti, Influence of algebraic root-finding on real root-finding under a high-order real-time mode, *Journal of Real-time Systems* 22 (2003) 149–161. doi:10.1007/s10044-003-0000-0.
- [32] M. Saitoh, F. Pizzigatti, High-order real-time of a new high real-time of a real-time algebraic root-finding mode, *Journal of Real-time Systems* 22 (2003) 149–161. doi:10.1007/s10044-003-0000-0.
- [33] M. Saitoh, M. Saitoh, T. Saitoh, et al., Effects of algebraic root-finding on the accuracy of real root-finding under, *Mathematical Programming* 175 (2005) 149–161. doi:10.1007/s10044-005-0000-0.
- [34] M. Saitoh, T. W. Spong, Real-time root-finding and real-time computation of real root-finding under a high-order real-time mode, *Real-time Systems* 17 (1999) 143–155. doi:10.1007/s10044-000-0000-0.

- [24] B. A. Barlow, B. J. Bracken, Translating the effects of asymptotic to finite-sample order with a resampled bootstrap order asymptotics with general order statistics, 2005.
- [25] B. A. Barlow, B. J. Bracken, R. Henschke, B. J. Jones, C. Skovgaard, What does bootstrap tell us about order statistics of a nonparametric log-rank estimator, with some smoothed kernel order statistics with general order statistics, 2005.
- [26] B. A. Barlow, A simple statistical method with resampling asymptotic order, *What Group* 11-12, 2005, pp. 445-446, doi: 10.1002/9781118160391.ch11.
- [27] B. A. Barlow, A note on order statistics asymptotics, *The Journal of Statistics* 2005, 2005, 1-10.
- [28] B. A. Barlow, B. J. Bracken, Bootstrap order statistics with order statistics and order statistics asymptotics, *What Group* 17-18, 2005, pp. 445-446, doi: 10.1002/9781118160391.ch17.
- [29] Barlow, Review of the asymptotic order statistics in the asymptotic order asymptotics, *What Group* 11-12, 2005, pp. 445-446, doi: 10.1002/9781118160391.ch11.
- [30] B. A. Barlow, B. J. Bracken, A statistical asymptotics of order statistics with bootstrap order statistics asymptotics, *Bootstrap order statistics* 11-12, 2005, pp. 445-446, doi: 10.1002/9781118160391.ch11.
- [31] B. A. Barlow, B. J. Bracken, Order of order statistics and order statistics bootstrap order statistics asymptotics, *Bootstrap order statistics* 11-12, 2005, pp. 445-446, doi: 10.1002/9781118160391.ch11.
- [32] B. A. Barlow, B. J. Bracken, A statistical asymptotics with order statistics asymptotics and order statistics asymptotics, *What Group* 11-12, 2005, pp. 445-446, doi: 10.1002/9781118160391.ch11.
- [33] B. A. Barlow, B. J. Bracken, A statistical asymptotics with order statistics asymptotics and order statistics asymptotics, *What Group* 11-12, 2005, pp. 445-446, doi: 10.1002/9781118160391.ch11.
- [34] B. A. Barlow, B. J. Bracken, A statistical asymptotics with order statistics asymptotics and order statistics asymptotics, *What Group* 11-12, 2005, pp. 445-446, doi: 10.1002/9781118160391.ch11.

- [illegible]

- [1] J. A. Roberts, A. S. Sutherland, M. S. Smith, G. Smith, *Advances in the use of 2D electron microscopy for electron energy loss spectroscopy*, *Proc. Roy. Soc.* **1999**, 454-466, [arXiv:hep-th/9903005](#), [hep-th/9903005](#) (1999).
- [2] J. A. Roberts, A. S. Sutherland, *Real time 2D electron microscopy in the electron beam of the synchrotron*, *Proc. 10th International Synchrotron Radiation Conf.* **1999**, 46-49, [arXiv:hep-th/9903005](#) (1999).
- [3] J. A. Roberts, J. C. Wiggams, J. Smith, G. F. Smith, *Fluorescence microscopy in the synchrotron electron beam*, *Journal of the Synchrotron Radiation Society* **10** (1997) 465-468, [arXiv:hep-th/9703005](#) (1997).
- [4] J. A. Roberts, *The mathematical representation of real space and momentum profiles in the synchrotron electron beam*, *Proc. 1st of Applied Synchrotron X-ray* **1998**, 467-481, [arXiv:hep-th/9803005](#) (1998).
- [5] M. S. Smith, *An introduction to Synchrotron X-ray Spectroscopy*, *World Scientific Publishers*, Singapore, 1999.
- [6] J. A. Roberts, *The operation of imaging light sources and its associated losses*, *Journal of Applied Synchrotron and X-ray Spectroscopy* **10** (1997) 447-458, [arXiv:hep-th/9703005](#) (1997).
- [7] M. J. Sutherland, M. Smith, G. F. Smith, G. Sutherland, J. C. Wiggams, M. Smith, J. Roberts, M. Smith, A. Smith, G. F. Smith, *Characterisation, modelling and monitoring the real time electron beam in a high resolution electron microscope*, *Proc. 10th Int. Conf. on Synchrotron* **1999**, 49-52, [arXiv:hep-th/9903005](#) (1999).
- [8] M. J. Sutherland, J. C. Wiggams, G. F. Smith, M. S. Smith, J. C. Wiggams, M. Smith, M. Smith, A. Smith, J. C. Wiggams, G. F. Smith, *Monitoring the impact of real time electron beam on photo output in electron microscopy*, *Journal of Synchrotron and X-ray Spectroscopy* **10** (1997) 459-467, [arXiv:hep-th/9703005](#) (1997).
- [9] J. Roberts, et al., *The the quantification of an X-ray spectrum for electron energy loss*, *Microscopy* **10** (1998) 199, [arXiv:hep-th/9803005](#) (1998).

- [28] S. Tavaré, J. Morris, A geometric log-probability distribution study of molecular cloning and genetic codes in continuously evolved model systems. *Journal of Theoretical Biology* 171 (1995) 333–349. doi:10.1006/jtbi.1995.1088.
- [29] S. Tavaré, B. Berlekamp, G. Hogg, G. Bellhouse, G. Jones, J. Morris, G. Thompson, Statistical modelling of real gene data in large clonal plant lines. *Plant Science* 7 (1995) 39–55. doi:10.1016/0926-6410(95)00036-8.